PHYSICAL REVIEW C VOLUME 32, NUMBER 3 SEPTEMBER 1985

^{198,199,200,201,202,204}Hg(n,γ) cross sections and the termination of s-process nucleosynthesis

H. Beer
Kernforschungszentrum Karlsruhe, Institut für Kernphysik III, D-7500 Karlsruhe 1, Federal Republic of Germany

R. L. Macklin
Oak Ridge National Laboratory, Oak Ridge, Tennessee 37830
(Received 29 November 1984)

The neutron capture cross sections of ^{198,199,200,201,202,204}Hg(n,γ) were measured in the energy range 2.6 to 500 keV. The average capture cross sections were calculated and fitted in terms of strength functions. Resonance parameters for the observed resonances were determined by a shape analysis. Maxwellian averaged capture cross sections were computed for thermal energies kT between 5 and 100 keV. The solar mercury abundance was determined to be 0.34 ± 0.04 relative to Si$=10^6$. The termination of s-process nucleosynthesis at lead and bismuth was investigated. The abundances of ^{206,207,208}Pb were reproduced introducing a strong fluence component of the s process in addition to normal s- and r-process nucleosynthesis. The radiogenic ^{207}Pb abundance was determined and the r-process age was calculated via ^{235}U. Using Fowler's exponential model, an age $T=4.6$ Gyr $+\Delta=17.2\pm2.6$ Gyr was obtained.

I. INTRODUCTION

One of the basic processes in the buildup of heavy elements, the slow neutron capture nucleosynthesis, terminates at the isotopes of lead and bismuth, where via the following α unstable nuclei all further neutron capture transformations are cycled back to the main isotopes of lead.

Just on the brink of this termination cycling the mercury isotopes are situated which form, therefore, the starting point for the s- and r-process analysis of lead and bismuth.

With regard to these considerations, it is unfortunate that mercury is a highly volatile element, the solar abundance of which could, therefore, hardly be determined via meteorite analyses.[1] However, the complete set of stable mercury capture cross sections from this work allows via s- and r-process systematics the unambiguous calculation of this quantity, which is in itself already of basic importance.

In the present study we display in Sec. II–IV the measurement and analysis of the stable mercury capture cross sections, and we give resolved resonance parameters and strength functions from a statistical model fit and Maxwellian averaged capture cross sections. In Sec. V the solar mercury abundance and a decomposition of the isotopic mercury abundances into its s and r contributions are presented.

Finally a calculation of the s-process path termination via Hg, Tl, Pb, and Bi is performed where the information deduced from the mercury isotopes is of basic importance. The calculations follow the concepts developed by Clayton and Rassbach[2] and Ward and Clayton.[3] The decomposition of the lead isotopes into the different nucleosynthetic contributions yielded the radiogenic ^{207}Pb abundance which was used to study the ^{235}U cosmic clock.

II. EXPERIMENTAL TECHNIQUE

A. Measurement

The mercury measurements were performed at the Oak Ridge Linear Accelerator (ORELA) in the neutron energy range 2.6–500 keV using the time-of-flight method. The accelerator repetition rate was adjusted to 500 and 800 Hz, respectively, for individual mercury samples, and an electron burst width of 5 ns full width at half maximum was maintained. The generated neutron beam from a water-cooled tantalum target[4] was filtered by ^{10}B (0.0269 atoms/b) to avoid an overlap of slow neutrons with the next neutron burst, and confined to a suitable beam profile at the sample position by a series of Cu collimators. The neutron burst from the target impinged on the sample to be investigated after a flight path of 40.12 m. The prompt capture gamma-ray cacade released by the capture event was counted by a pair of hexafluorobenzene (C_6F_6) scintillation detectors placed symmetrically outside the neutron beam and viewing the sample edge on. The neutron beam was monitored by a 0.5 mm thick ^{6}Li glass detector 430 mm in front of the sample. The stability of this detector was frequently checked by a ^{241}Am α source.

The mercury samples consisted of HgO powder pressed to tablets of quadratic dimensions (26×26 mm) by means of Lucite powder as a binder. The individual sample characteristics are listed in Table I. The samples were exposed to the neutron beam in a 6.4 μm thick Mylar foil bag.

The capture events were accumulated two-dimensionally into 128 pulse height and 18 000 time-of-flight channels. For the pulse height a sharp digital threshold was set at 153 keV.

The time-of-flight data were collected in four different sections with 1, 2, 4, and 8 ns per channel. The energy calibration of the time-of-flight channels was performed

TABLE I. Hg sample characteristics.

Main isotope	Weight HgO (mg)	Lucite added (mg)	Thickness d[a] (cm)	Isotopic compositions (%)[b] 198	199	200	201	202	204
198	2141	238	0.07	75.51	6.98	6.09	3.14	6.77	1.52
199	1052	117	0.04	1.58	91.48	4.97	0.76	1.05	0.16
200	3442	383	0.11	2.58	6.48	74.83	5.43	9.33	1.35
201	1715	191	0.055	0.24	0.52	3.12	89.00	6.70	0.42
202	3172	352	0.095	0.06	0.17	0.53	1.38	97.58	0.28
204	4655	517	0.145	0.07	0.14	0.26	0.23	1.10	98.20

[a]The dimensions of the samples were $2.6\times2.6\times d$ cm.
[b]The content on ^{196}Hg was $\leq 0.05\%$.

by well-known resonances in ^{27}Al at 5.903 keV and 1.094 MeV. The pulse height scale was frequently checked with the Compton edge of the 4.43 MeV gamma line of a PuBe source whose total count rate was also used to check the stability of the detector efficiency.

B. Pulse height weighting and flux normalization

In order to derive the total capture cross section from the measurement of the prompt gamma radiation, the recorded capture event must be independent of the details of the cascade. This is achieved by pulse height weighting.[5,6] This procedure results in an efficiency of the detectors which is proportional to the excitation energy (neutron separation energy plus center of mass energy of the incident neutron). The capture events $C(I)$ were multiplied by the weighting function $W(I)$ and summed over the pulse height channels I. As the sample in practice is not isotopically pure (Table I), the resulting quantity is related to all isotopic mercury capture cross sections σ_j by the following expression:

$$\sum C(I)W(I)=k\Phi N\mathrm{MS}K_\gamma \sum_j \sigma_j H_j E_j^* \ , \tag{1a}$$

with the excitation energy

$$E_j^*=E_{Bj}+E_n\frac{A}{A+1} \ . \tag{1b}$$

k is a normalization constant, Φ the neutron flux, N the total number of mercury atoms, MS the correction factor for neutron multiple scattering and self-shielding, and K_γ the correction for gamma-ray self-absorption in the sample. H_j designates the abundance of isotope j and E_{bj} the respective neutron separation energy, E_n is the neutron kinetic energy, and A is the target mass number. In order to obtain a detector efficiency proportional to the excitation energy E^*, the weighting function $W(I)$ has to fulfill the following equation:

$$\sum_i \sum_I P(E_{\gamma i})S(E_{\gamma i},I)W(I)=k\sum_i E_{\gamma i}=kE^* \ , \tag{2}$$

where P is the interaction probability of a gamma ray of energy $E_{\gamma i}$ and S is the probability that it will produce a pulse of height I in the detector. S and W are specific properties of the detection system given elsewhere.[7] The normalization constant k is determined by means of the saturated resonance technique using the 4.9 eV resonance of ^{197}Au.[8] For this resonance we can write, according to Eq. (1a),

$$\sum_I C_{\mathrm{Au}}(I)W(I)=k\Phi(E_n=4.9\,\mathrm{eV})Y_{\mathrm{Au}}E^*_{\mathrm{Au}} \ , \tag{3}$$

where Y_{Au} is the gold capture yield. As for this resonance with $\Gamma_\gamma \gg \Gamma_n$, the capture yield of a sample of 0.0029 atoms/b is effectively one because virtually all neutrons are captured, we can normalize the neutron flux determined via the observed yield of the ^{6}Li glass monitor:

$$k\Phi(E_n)=\frac{k\Phi(E_n=4.9\,\mathrm{eV})}{Y_{\mathrm{Li}}(E_n=4.9\,\mathrm{eV})}Y_{\mathrm{Li}}(E_n) \ . \tag{4}$$

As the normalization procedure is dependent on the discriminator settings of the associated electronics, it is periodically reevaluated, especially when the PuBe source calibrations indicate a significant change in detector efficiency.

III. DATA REDUCTION

Before addition of the capture events to the stored data, the linear pulse of the detector was transmitted to an on-line computer to perform the pulse height weighting. For the final stored data in the first step the flight time scale was converted to an energy scale. The data were corrected for dead time and the background events were subtracted. The accelerator-independent background was calculated in two ways: (i) from the time interval where the ^{10}B filter is nearly black and (ii) from the periods where the accelerator was off. The accelerator-dependent background was obtained from several runs with no sample in the neutron beam and the time-independent background subtracted. Additional background from neutrons scattered in the sample and captured in the structural material of the detection system (fluorine of the scintillator, Al housing of the detectors) was taken into account firstly as a subtracted background proportional to the potential scattering of the sample and secondly for individual resonances using the tabulated correction factors.[9] Further corrections to be determined were neutron multiple scattering and self-shielding[10] and the gamma absorption of the cascade in the sample. (Typical values for these corrections are given in Table VIII).

TABLE II. ^{198}Hg(n,γ) resonances. The stated uncertainty is statistical only.

E_0 (eV)	$\frac{g\Gamma_n\Gamma_\gamma}{\Gamma}$ (meV)	E_0 (eV)	$\frac{g\Gamma_n\Gamma_\gamma}{\Gamma}$ (meV)
3 122	13.4± 1.8	7 055	78.2± 9.0
3 131	32.6± 3.1	7 157	31.7± 4.8
3 138	46.3± 1.6	7 253	24.3± 6.2
3 271	61.5± 1.6	7 485	24.5± 6.7
3 294	7.1± 1.6	7 518	144.4±11.1
3 383	108.7± 2.0	7 557	23.7± 7.0
3 626	10.3± 1.6	7 613	132.5±11.7
3 638	35.5± 2.6	7 846	60.4± 8.5
3 797	95.5± 2.0	7 865	81.3± 9.3
3 911	8.3± 1.5	8 100	137.0±11.0
4 152	79.5± 4.9	8 146	26.0± 6.6
4 282	10.8± 2.5	8 296	25.1± 6.2
4 313	76.0± 4.6	8 411	110.7±10.1
4 359	14.9± 2.9	8 467	115.1±11.6
4 553	93.3± 5.8	8 584	63.2±12.5
4 673	106.7± 4.9	8 598	77.0±10.3
4 703	9.7± 2.2	8 777	60.8± 9.0
4 769	24.3± 2.7	8 796	71.4± 9.4
4 878	13.4± 2.1	8 843	163.1±12.7
4 963	53.9± 3.8	9 082	87.1±11.3
5 183	109.9± 5.3	9 670	41.1± 9.7
5 488	96.2± 5.9	9 698	80.4±13.7
5 641	111.3± 6.1	9 719	70.9±12.2
5 763	98.0± 6.1	9 928	100.3±11.9
5 889	34.1± 6.9	10 278	74.7±10.8
6 174	65.8± 5.7	10 477	88.9±10.0
6 201	21.8± 3.8	10 497	83.2±11.6
6 343	64.5± 6.5	10 786	109.6±11.7
6 452	19.7± 4.0	10 877	74.8±10.3
6 528	22.1± 3.7	11 111	67.8±15.1
6 561	99.6± 7.7	11 127	84.4±11.8
6 645	29.7± 3.9	11 462	110.4±13.5
6 689	93.6± 6.7	11 616	76.3±11.6
6 982	15.0± 5.1	11 734	23.7± 8.5

TABLE III. ^{199}Hg(n,γ) resonances. The stated uncertainty is statistical only. (d) indicates a probable doublet or multiplet.

E_0 (eV)	$\frac{g\Gamma_n\Gamma_\gamma}{\Gamma}$ (meV)	$g\Gamma_n$ (eV)	Γ_γ (meV)
3088	155.8± 2.8		
3170	40.8± 1.6		
3212	143.3± 2.9		
3234	144.5± 2.9		
3325	157.0± 2.9		
3469	13.1± 1.5		
3543	127.5± 2.8		
3562	49.5± 2.0		
3607	129.8± 3.0		
3714	175.2± 4.0		
3741	92.5± 2.8		
3795	4.2± 4.0		
3797	11.5± 3.5		
3856	34.3± 2.0		
3970	131.9± 3.5		

TABLE III. (*Continued*).

E_0 (eV)	$\frac{g\Gamma_n\Gamma_\gamma}{\Gamma}$ (meV)	$g\Gamma_n$ (eV)	Γ_γ (meV)
4015	69.8± 8.3	6.0±1.0	283.5±34.0
4088	125.4± 3.6		
4160	149.0± 3.9		
4194	13.2± 1.6		
4342	26.7± 1.9		
4365	168.0± 5.1		
4371	18.9± 4.5		
4414	156.3± 3.5		
4434	22.0± 1.6		
4508	21.2± 1.8		
4559	108.9± 3.7		
4571	130.4± 3.9		
4661	68.7± 2.6		
4786	117.7± 3.4		
4847	65.2± 2.8		
4956	157.1± 3.9		
4994	160.1±10.1	8.41±0.73	218.0±13.8
5092	23.9± 1.9		
5118	125.7± 3.3		
5207	78.3± 2.8		
5374	104.3± 3.4		
5389	38.4± 2.8		
5486	145.4± 3.9		
5612	19.0± 2.2		
5633	51.8± 2.8		
5686	141.2± 4.5		
5779	184.9± 11.6	4.52±0.48	257.7±17.3
5957	105.9± 4.3		
6011	34.0± 2.8		
6081	15.6± 2.4		
6147	40.1± 4.8		
6158	105.4± 4.5		
6314	104.7± 4.2		
6403	54.2± 3.8		
6437	184.5± 5.9		
6480	132.7± 5.0		
6565	64.1± 3.9		
6626	54.1± 4.0		
6726	79.3± 4.3		
6774	127.9± 5.2		
6851	41.0± 4.3		
6869	128.7± 5.6		
6916(d)	98.0±12.9		
6989	138.3± 6.1		
7051	143.0± 6.1		
7176	25.6± 3.4		
7259	260.2± 25.2	19.2±2.5	361.1±32.4
7323	98.6± 5.7		
7490	129.9± 5.4		
7568	177.2± 6.8		
7753	172.2± 7.0		
7769	89.2± 5.5		
7789	54.6± 4.4		
7920	178.3± 7.0		
8018	97.2± 5.4		
8117	175.9± 7.0		
8159	147.3± 6.2		
8282	18.9± 4.5		

TABLE III. (*Continued*).

E_0 (eV)	$\frac{g\Gamma_n\Gamma_\gamma}{\Gamma}$ (meV)	$g\Gamma_n$ (eV)	Γ_γ (meV)
8305	142.7± 6.4		
8361	148.3± 6.5		
8398	30.1± 3.8		
8472	131.2± 6.2		
8510	17.0± 3.6		

TABLE IV. ^{200}Hg(n,γ) resonances. The stated uncertainty is statistical only.

E_0 (eV)	$\frac{g\Gamma_n\Gamma_\gamma}{\Gamma}$ (meV)	$g\Gamma_n$ (eV)	Γ_γ (meV)
2 871	9.5±1.6		
2 881	14.9±1.0		
2 911	13.1±1.7		
2 942	9.7±1.8		
3 015	11.4±1.7		
3 038	12.0±2.0		
3 251	82.8±2.2		
3 355	7.9±2.0		
3 764	87.0±2.1		
4 274	51.1±3.9		
4 303	70.5±4.9		
4 569	12.0±3.3		
4 682	18.3±2.3		
4 812	10.0±2.3		
4 992	13.9±3.4		
5 018	30.2±5.6		
5 024	77.2±7.6		
5 032	43.1±5.2		
5 174	30.2±3.6		
5 249	313.4±19.2	1.91±0.15	375±32
5 374	8.7±2.9		
5 858	51.3±6.8		
6 046	20.8±5.0		
6 174	47.3±6.7		
6 220	106.1±10.3		
6 722	170.7±14.4		
6 765	44.6±6.8		
7 241	47.0±7.6		
7 679	26.6±7.1		
7 991	347.0±38.0	41.4±5.1	350±39
8 253	367.0±29.0	12.4±1.4	378±31
8 677	50.6±8.5		
8 845	39.5±9.5		
8 939	234.2±20.1	2.0±0.4	265±26
9 013	87.5±10.8		
9 173	122.0±13.1		
9 745	35.7±11.6		
10 193	50.5±13.2		
10 530	238.3±24.8		
10 979	107.4±19.1		
11 004	57.9±16.1		

TABLE V. ^{201}Hg(n,γ) resonances. The stated uncertainty is statistical only. (d) indicates a probable doublet or multiplet.

E_0 (eV)	$\frac{g\Gamma_n\Gamma_\gamma}{\Gamma}$ (meV)	$g\Gamma_n$ (eV)	Γ_γ (meV)
3 235	193.0± 6.0	2.58±0.14	393±14
3 455	5.0± 1.3		
3 517	5.2± 1.3		
3 562	236.0± 7.0	3.0 ±0.17	482±18
3 719	76.6± 5.3		
3 792	157.0± 6.5	4.17±0.30	308±14
3 933	12.4± 4.4		
3 945	164.0± 7.5	6.47±0.45	317±16
4 069	105.5± 5.3		
4 121	19.8± 3.6		
4 128	26.6± 3.2		
4 246	146.0± 6.0	1.0 ±0.1	322±16
4 278	157.4± 6.4	3.0 ±0.3	313±14
4 297	5.6± 2.2		
4 375	15.3± 2.7		
4 385	40.9± 3.4		
4 494	127.8± 5.6		
4 624	27.6± 3.1		
4 773	54.9± 4.4		
4 950	208.0±11.0	1.26±0.10	470±35
4 965	47.6± 3.9		
5 149	36.7± 5.2		
5 158	62.5± 5.0		
5 214	96.9± 1.8		
5 362	112.3± 1.4		
5 391	15.0± 2.6		
5 492	20.1± 3.8		
5 582	125.1±10.4	0.93±0.10	272±29
5 771	101.1±83.1		
5 913	110.4±23.8	0.75±0.33	243±77
5 969(*d*)	305.0±14.0	7.11±0.60	601±31
6 277	187.7±12.4	1.0	435±35
6 299	28.5± 5.1		
6 390	175.9±12.0	1.0	402±33
6 698	66.5± 7.4		
6 891	171.9±13.0	1.0	391±36
6 906	115.1±13.0	1.0	245±31
6 921	36.9± 7.9		
7 113	137.7±11.0	1.0	301±28
7 136	140.8±11.8	1.0	309±30
7 223	183.6±13.4	1.0	424±38
7 338	18.6± 5.1		
7 365	174.2±12.8	1.0	397±35
7 599	53.0± 7.8	1.0	105±16
7 716	29.3±10.9		
7 728	70.1±12.4	2.0	137±25
7 807	48.1± 7.0	1.5	98±14
7 928	102.7±14.9	1.52±0.31	207±35
7 964	24.9± 6.0		
8 049	23.1± 5.3		
8 104	44.3± 8.7	1.62±0.36	86±18
8 157	95.8±14.8	1.19±0.25	196±36
8 399	200.8±19.4	1.36±0.19	443±59
8 687	47.5± 7.0		
8 781	48.4± 7.8		
8 831	103.7±10.3		
8 915	77.7± 9.4		
8 946	51.8± 9.0		

TABLE V. (*Continued*).

E_0 (eV)	$\frac{g\Gamma_n\Gamma_\gamma}{\Gamma}$ (meV)	$g\Gamma_n$ (eV)	Γ_γ (meV)
9075	261.4±19.0	3.43±0.41	533±44
9097	25.8± 9.3		
9225	236.1±19.3	2.85±0.35	485±46
9435	59.5± 9.4		
9458	37.7± 6.9		
9483	79.9±10.3		
9591	210.5±23.0	1.16±0.18	484±78
9794	53.5± 8.7		
9965	181.2±14.7	1.2	402±38
10006	75.4±10.1		
10026	70.1±10.4		
10193	56.3± 9.1		
10221	135.9±12.3		
10385	141.5±13.1	0.9	316±35
10422	88.8±11.3		
10644	107.3±10.7		
10906	147.2±14.6		
10945	225.8±17.8	1.2	524±51
11012	207.8±16.3	1.2	473±45
11049	284.6±19.2	1.2	703±62

TABLE VI. ^{202}Hg(n,γ) resonances. The stated uncertainty is statistical only.

E_0 (eV)	$\frac{g\Gamma_n\Gamma_\gamma}{\Gamma}$ (meV)	$g\Gamma_n$ (eV)	Γ_γ (meV)
3890	23.0± 0.9		
4087	20.3± 1.1		
4167	655.0± 17.0	11.8±0.4	694±19
7427	101.2± 9.2		
7829	71.9± 7.3		
7881	72.2± 8.7		
8961	68.4± 12.2		
8977	247.9± 16.0		
8994	71.1± 12.1		
9600	34.3± 15.6		
9615	531.8± 10.8		
11421	106.5± 13.2		
14194	48.5± 21.6		
14244	749.2± 59.4	24.7±3.3	773±63
14743	63.8± 19.0		
16421	174.7± 19.2		
16652	183.7± 19.8		
16773	255.8± 25.0		
17344	75.2± 17.8		
18565	135.4± 23.7		
24405	217.5± 30.8		
24727	114.0± 20.6		
25309	661.5± 54.4		
25969	297.1± 40.5		
26693	106.5± 25.2		
28426	380.4± 57.1		
28690	196.8± 48.4		
29410	170.8± 40.6		
30882	404.3± 58.4		
31415	234.8± 46.9		

TABLE VI. (*Continued*).

E_0 (eV)	$\frac{g\Gamma_n\Gamma_\gamma}{\Gamma}$ (meV)	$g\Gamma_n$ (eV)	Γ_γ (meV)
32 643	277.0 ± 49.5		
32 730	260.7 ± 54.5		
35 367	179.2 ± 68.4		
37 332	345.6 ± 93.3		
37 401	386.3 ± 80.8		
39 413	858 ± 108		

TABLE VII. ^{204}Hg(n,γ) resonances. The stated uncertainty is statistical only.

E_0 (eV)	$\frac{g\Gamma_n\Gamma_\gamma}{\Gamma}$ (meV)	$g\Gamma_n$ (eV)	Γ_γ (meV)
5 996	18.2± 3.6		
6 015	133.5± 2.5		
7 710	1 867 ± 75	93.0±3.1	1 905± 76
9 282	108.3± 8.2		
14 318	182.9± 15.0		
16 730	168.7± 13.4		
22 060	157.4± 15.9		
24 777	89.5± 17.6		
26 570	102.5± 22.3		
31 515	203.6± 27.7		
47 010	442.8± 67.4		
47 154	1 212 ±120		
62 105	2 196 ±353	30.2±6.8	2 369±441
62 757	2 106 ±341	26.7±5.8	2 294±437
63 920	568 ±137		
70 013	2 558 ±337	30.0±6.0	2 796±403
70 551	889 ±160		
82 742	850 ±187		
85 328	3 450 ±553	45.9±9.1	3 731±680
86 639	1 205 ±310		
92 877	1 858 ±375	30.0±6.0	1 980±426
93 308	815 ±304		
97 910	1 760 ±383		

The data reduction according to Eq. (1a) first yields an effective capture cross section σ_{eff} which is related to the isotopic cross sections by

$$\sigma_{\text{eff}}=\sigma_x+\sum_j H_j\sigma_j E_j^*/H_x E_x^* , \tag{5}$$

where x stands for the highly enriched isotope of the investigated sample to be determined. The samples used are thin enough that this linear approximation (omitting resonance saturation effects) is adequate in the energy range studied. The application of the excitation energy E_x^* at this step of analysis instead of an effective excitation energy has the advantage that in the resolved resonance region, the outstanding resonances of this main isotope are already correctly treated. As enriched samples of all six stable mercury isotopes except the very rare ^{196}Hg were measured and analyzed, the matrix implied by Eq. (5) could be inverted exactly to unscramble the individual isotopic capture cross sections we report.

IV. DATA ANALYSIS

A. Individual resonances

The level spacing of the mercury isotopes and the energy resolution of ORELA were sufficient to resolve individual resonances for all isotopes from 2.6 keV up to 100 keV for the isotope closest to nuclear shell closure, ^{204}Hg. For a large number of resonances the total widths are found to be narrow compared to our energy resolution. Therefore only the quantity $g\Gamma_n\Gamma_\gamma/(\Gamma_n+\Gamma_\gamma)$, which is proportional to the resonance area, could be extracted for these resonances. g designates the statistical spin factor $(2J+1)/[2(2I+1)]$ with compound nucleus spin J and target spin I. Γ_n and Γ_γ are the neutron and radiation widths, respectively. For some resonances where $\Gamma_n+\Gamma_\gamma$ is larger than about an eighth of our resolution, separate values of $g\Gamma_n$ and Γ_γ could be extracted with some confi-

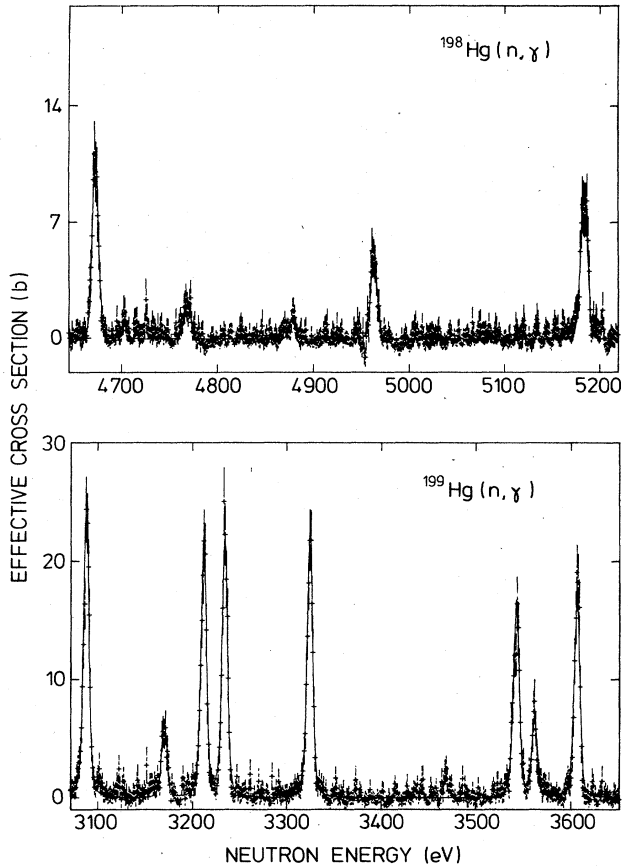

FIG. 1. Samples of ^{198,199}Hg(n,γ) yield data. The solid line is generated from the least squares fitting code LSFIT (Ref. 11) to extract resonance parameters. The fit is performed including Dopper broadening, resonance self-protection, multiple scattering, and both Gaussian and exponential resolution functions.

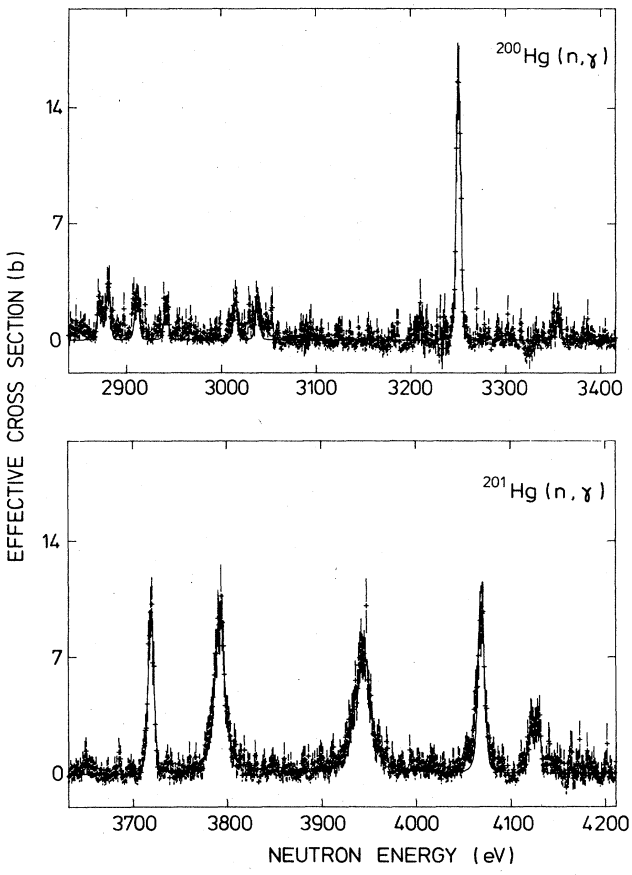

FIG. 2. Samples of ^{200,201}Hg(n,γ) yield data. For information about the fitting procedure (solid line) see Fig. 1.

dence.

The resonance analysis was performed with the computer code LSFIT (Ref. 11), which provides a least squares fit of the resonances to a sum of Breit-Wigner single or multiple forms. Resonance energies, and $g\Gamma_n\Gamma_\gamma/(\Gamma_n+\Gamma_\gamma)$ or $g\Gamma_n$ and Γ_γ values for the individual isotopes, are given in Tables II—VII. Resonances marked with a *d* are suspected to be multiplets according to an asymmetric shape of the observed peak. A few illustrations of the fits obtained are shown in Figs. 1—3.

B. Average capture cross sections

For the determination of the effective mercury cross sections in the whole measured energy region, the sample yield data were binned to smear out individual resonance fluctuations. This procedure provides adequate data for a parametrization in terms of strength functions. The computer code FITACS (Ref. 12) was used for this kind of parametrization.

The effective capture cross sections of the individual isotopes averaged over various energy intervals are given in Table IX. Figures 4 and 5 show the statistical model fits of the average cross sections, and the average resonance parameters of these fits are summarized in Table X.

C. Systematic uncertainties

Systematic uncertainties originate mainly from the saturated resonance technique and the shape of the ^{6}Li(n,α) cross section, procedures essential to create an absolute capture cross section. Other important uncertainties inherent to the method come from the pulse height weighting technique, the corrections for multiple scattering and self-shielding, and the correction for gamma-ray absorption in the sample. The various uncertainties are summarized in Table VIII. A detailed consideration of the uncertainties in flux determination as a function of neutron energy has been given recently.[13]

D. Maxwellian averaged capture cross sections

Maxwellian averaged capture cross sections $\langle\sigma v\rangle/v_T$ were calculated from differential data by numerical integration according to

TABLE VIII. Corrections and uncertainties.

	Correction (%)	Uncertainty (%)
Saturated resonance calibration		3
Shape of ^{6}Li (n,α) cross section		
at 50 keV		1
at 250 keV		2
Pulse height weighting technique		1
Neutron sensitivity	(198)25	(198)3.2
of detection system	(199)10	(199)1.6
for averages over unanalyzed resonances	(200)44	(200)6.5
around 30 keV[a]	(201)18	(201)2.3
	(198)66	(198)6.8
	(199)51	(199)4.5
Background subtraction	(200)64	(200)6.6
	(201)42	(201)2.3
Dead time	≤ 1.2	<0.02
Neutron multiple scattering and self-shielding for averages over unanalyzed resonances around 30 keV	0.6—1.1	0.1—0.2
Gamma-ray self-absorption	0.9—3.5	≤ 0.3
Detector bias extrapolation ($E_{bias}=153$ keV)	assumed same as for weighted calibration	0.4
Misalignment of sample		<0.2
Uncertainty in detector efficiency by gain drifts of electronics		<0.4
Resonance shape (unknown spin, resolution function)		<3

[a]For individual resonances (e.g., Table VII 7710 eV) $\leq 6\%$ correction with uncertainty of half the correction included in quadrature in the parameter table.

TABLE IX. Histogram of the average neutron capture cross sections of ^{198,199,200,201,202,204}Hg.

E_n (keV)	σ (mb) 198	199	200	201	202	204
3	496.1	1489.8	290.4	1232.0		
4	402.5	1238.3	286.8	1041.3	312.3	45.5
6	340.1	938.8	190.8	881.0	91.9	631.2
8	258.7	753.7	278.1	617.6	247.3	136.0
10	247.4	607.6	148.8	584.0	119.7	48.1
15	179.0	432.7	91.7	467.3	69.8	39.6
20	141.6	350.2	113.3	339.6	66.5	61.3
30	127.1	262.5	88.6	226.2	51.7	30.7
40	142.2	281.6	82.8	172.3	81.9	38.4
60	126.0	248.5	93.8	129.7	58.9	42.4
80	103.8	222.6	80.7	100.4	70.8	27.9

TABLE IX. (*Continued*).

E_n (keV)	198	199	200	201	202	204
			σ (mb)			
100	117.9	212.0	78.8	79.0	43.9	26.6
150	114.4	172.2	72.6	67.0	48.8	30.3
200	116.2	100.3	54.1	53.9	38.0	19.9
300	109.7	73.7	60.2	46.2	36.6	16.0
400	95.4	73.3	43.7	45.0	39.3	12.3
500						

TABLE X. Average resonance parameters from a statistical model fit.

Target nucleus A_Z	Strength function $S_l \times 10^4$ $l=1$	$l=2$	$l=3$	$\Gamma_{\gamma l}/D_l \times 10^4$ $l=1$	$l=2$
^{198}Hg	0.43±0.20	0.12±0.04	0.38±0.13	8 ±2	38 ±10
^{199}Hg	2.68±0.33	0.46±0.03	0.08±0.03	21 ±2	74 ± 7
^{200}Hg	0.13±0.06	0.15±0.07	0.15±0.07	6.3±0.3	10.7± 0.6
^{201}Hg	2.65±0.43	0.75±0.15	2.21±0.62	24 ±3	49 ± 7
^{202}Hg	0.17±0.31	0.12±0.10	0.17±0.13	2.5±0.2	7.4± 0.3

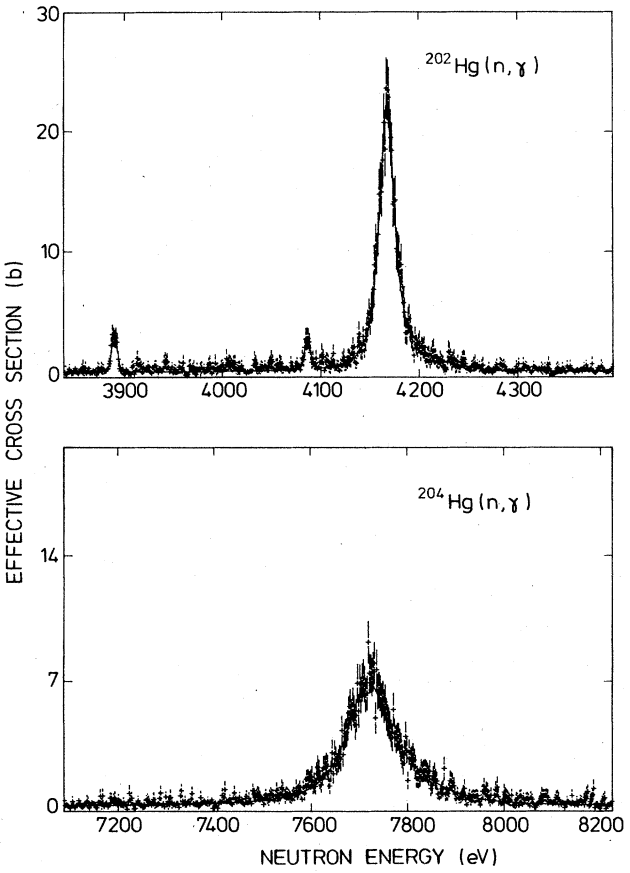

FIG. 3. Samples of ^{202,204}Hg(n,γ) yield data. For information about the fitting procedure (solid line) see Fig. 1.

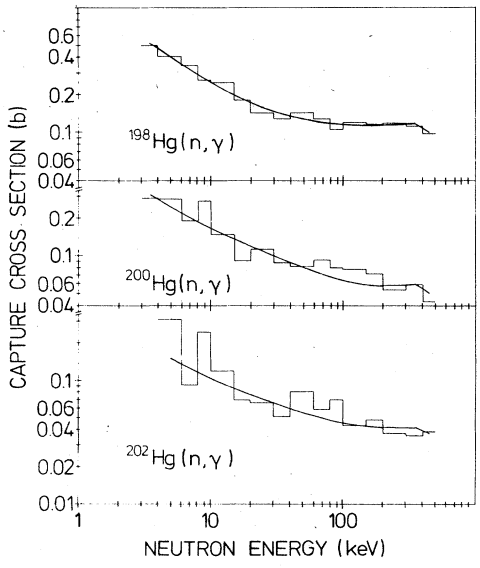

FIG. 4. Effective cross sections of ^{198,200,202}Hg(n,γ). The curves are a statistical model fit to the data.

$$\frac{\langle \sigma v \rangle}{v_T} = \frac{2}{\sqrt{\pi}} \int_0^\infty \sigma(E_n) E_n \exp(-E_n/kT) dE_n / \int_0^\infty E_n \exp(-E_n/kT) dE_n \ . \quad (6)$$

For the present range of temperatures ($kT = 5-100$ keV), it is sufficient to carry out the integration over the limited energy interval below 500 keV without essential errors. The integration was performed in two steps corresponding to the cross section regions of resolved and unresolved resonances. For the range of resolved resonances it was convenient to use resonance parameters instead of the differential cross section. The corresponding modification of Eq. (6) for this case was taken from Macklin and Gibbons.[14] The results of our calculations for $\langle \sigma v \rangle / v_T$, which in the following discussion will be simply designated as σ, are summarized in Table XI.

V. DISCUSSION

A. The solar mercury abundance

Mercury is one of few elements for which no reliable experimental data on its solar abundance are available, neither from meteorites nor from the spectrum of the sun.[1,15] The isotopic abundances given by Anders and Ebihara,[1] Cameron,[16] and Palme *et al.*[17] are calculated by interpolation between neighboring elements. A more reliable procedure has been used by Walter and Beer[18] based on the σN systematics of the s process. Normally the isotopic solar mercury abundances $N_\odot$ are a mixture of two processes of nucleosynthesis, the s process with abundance N_s and the r process with abundance N_r. Only for ^{198}Hg, a pure s-process nuclide (Fig. 6), are σN systematics which refer to the s process directly applicable. As the capture cross section of ^{198}Hg was not measured, the $(s+r)$ isotope ^{202}Hg had to be used in conjunction with a reasonable r-process correction.

In this work the determination of the solar mercury abundance via the σN systematics with a measured ^{198}Hg capture cross section is straightforward. A σN analysis based on newly evaluated cross sections and abundances has been carried out by Beer *et al.*[19] [Fig. 9(a)]. According to this calculation we get N_s (^{198}Hg)= (0.034 $\pm$0.004)/10^6 Si and therefore $N_\odot$(Hg)=(0.34$\pm$0.04)/ 10^6 Si. This result is 30% higher than the value derived by Walter and Beer.[18] This difference mainly comes from a revision of the σN curve.[19] The analysis of Walter and Beer[18] had to rely on a $\sigma N(A)$ calculation[20] which was not yet updated concerning new cross sections and solar abundances.[1,19]

The mercury isotopes ^{199,200,201,202,204}Hg are chiefly a mixture of $(s+r)$-process abundances besides an $\sim$1% p-process contribution. The capture cross sections in conjunction with the respective $\sigma N(A)$ values can be used to decompose the isotopic abundances into their s- and r-process contributions. The r-process abundance follows from the solar abundance minus the s-process abundance which is obtained from the $\sigma N(A)$ values divided by the capture cross section. Table XII summarizes these results.

B. Termination of the s process

The termination of the s process is illustrated in Fig. 6. The isotopes of Hg and Pb and isotopes in their vicinity are shown in a section of the chart of nuclides. The s process path is represented by a solid line. Up to mass number $A = 205$ the abundances of the stable isotopes are pre-dominantly a mixture of the common $(s+r)$ process. At ^{203}Hg ($T_{1/2}$=46.59 d), ^{204}Tl ($T_{1/2}$=3.78 yr), and ^{205}Pb ($T_{1/2}=1.5\times10^7$ yr), branchings of the s process can occur the absolute size of which is dependent on the s-process temperature and neutron density.

The situation is much more complicated at the stable isotopes ^{206,207,208}Pb and ^{209}Bi. The s-process path is ter-

TABLE XI. Maxwellian averaged capture cross sections of the stable mercury isotopes as a function of thermal energy kT.

Thermal energy kT (keV)	$\langle \sigma v \rangle / v_T$ (mb)					
	198	199	200	201	202	204
5	588	1348	324	950	179	93
10	318	755	198	593	106	63
15	240	561	155	446	87	51
20	205	467	135	361	80	46
25	186	411	123	305	77	44
30	173±15	374±23	115±12	264±14	74±6	42±4
35	165	346	110	234	72	40
40	159	325	106	211	70	39
45	154	307	102	192	68	38
50	150	291	99	177	66	37
70	142	244	90	137	61	33
100	135	198	80	106	55	29

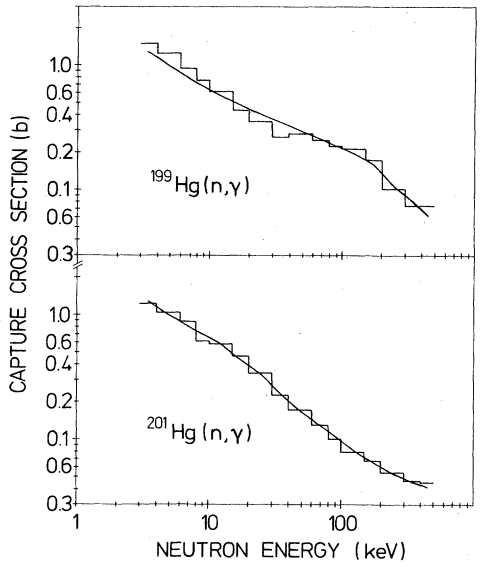

FIG. 5. Effective cross sections of ^{199,201}Hg(n,γ). The curves are a statistical model fit to the data.

minated at ^{210}Bi ($T_{1/2}=5$ d), and the *s*-process flow is cycled back via the ^{210}Po or ^{211}Po α decay to ^{206}Pb or ^{207}Pb, respectively. Whether the α decay of ^{211}Po is a strong alternative to the α decay of ^{210}Po ($T_{1/2}=138$ d) depends on the neutron density and the resulting *s*-process capture time of ^{210}Po. Another possibility to partially bypass ^{206}Pb in the α recycling exists through an isomeric state in ^{210}Bi^m ($T_{1/2}=3\times10^6$ yr) which is significantly populated by neutron capture of ^{209}Bi. If this initial population is *not quickly* destroyed in the hot stellar *s*-process environment by induced electromagnetic transitions, neutron capture to ^{211}Bi and subsequent α and β decays lead to ^{207}Pb.[2,3]

In Fig. 6 it is indicated that there are three *r*-process contributions to the abundances of ^{206,207,208}Pb and ^{209}Bi: direct, short-lived transbismuth nuclei and long-lived decay of ^{232}Th and ^{235,238}U.

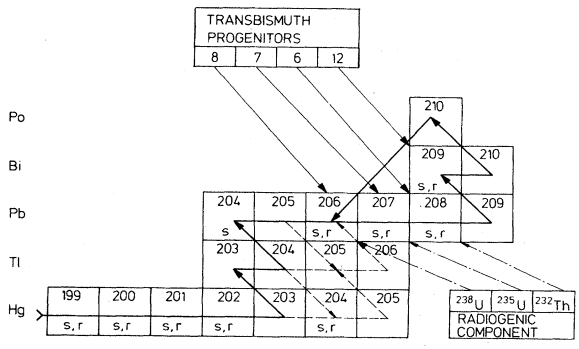

FIG. 6. Section of the chart of nuclides around Hg and Pb to illustrate the *s*-process termination with α recycling and the special *r* process and radiogenic U and Th components to ^{206,207,208}Pb and ^{209}Bi.

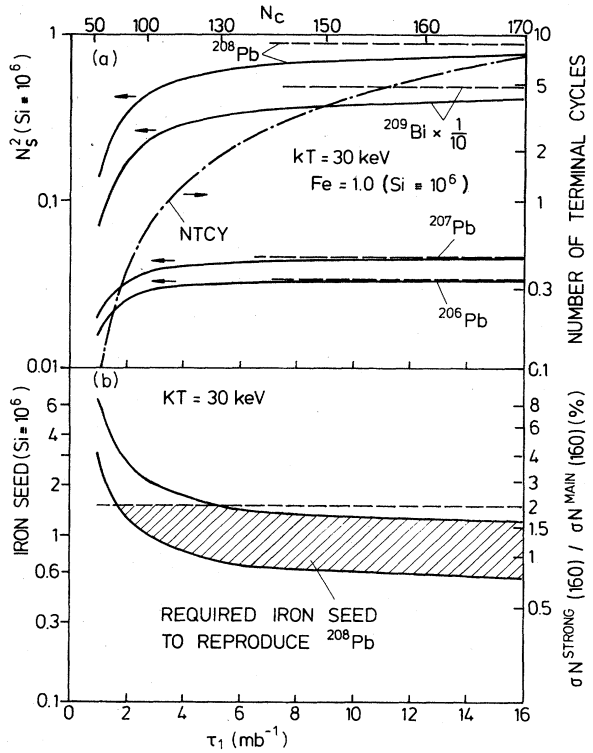

FIG. 7. (a) The ^{206,207,208}Pb and ^{209}Bi abundances and the corresponding number of terminal cycles (NTCY) are given as a function of τ_1 for $kT=30$ keV and an iron seed $f_1 N_\odot$ (^{56}Fe)$=1.0/10^6$ Si. The average number of captured neutrons N_c is indicated on the upper scale. (b) The iron seed required to reproduce the strong ^{208}Pb *s*-process component is shown as a function of τ_1. On the right-hand scale the percentage of the strong *s*-process component relative to the main component for $A<206$ is given. A contribution below 2% as indicated by the dashed line is within the uncertainty of the main *s*-process component ($\pm4\%$).

^{206,207,208}Pb have eight, seven, and six short-lived transbismuth progenitors and radiogenic components from ^{238}U, ^{235}U, and ^{232}Th, respectively, the sizes of which depend on the age of the *r*-process nucleosynthesis. The situation at ^{209}Bi is somewhat different; the number of progenitors including ^{237}Np ($T_{1/2}=2.14\times10^6$ yr) is ~12, the exact value depending on the fission cutoff of the *r* process.[29]

As the transbismuth elements which lie in the *r*-process valley following the 126-neutron *r*-process peak at osmium are expected to show no outstanding structures besides fluctuations like the odd-even staggering, the total *r*-process yield of ^{206,207,208}Pb and ^{209}Bi is simply calculated by multiplying the direct *r*-process components of the lead isotopes and of ^{209}Bi with the number of short-lived transbismuth progenitors. The specific *r*-process component of ^{206,207,208}Pb and ^{209}Bi is obtained by extrapolating the relatively constant average level of *r*-process abundances reached at $A\sim204$ to the mass numbers $A=206$

TABLE XII. Isotopic abundances decomposed according to their nucleosynthetic s process and r process and radiogenic origin. For $A<206$, N_s^1, the main component, is practically identical with N_s. N_s^2 designates the strong s process component, N_r the r-process abundance, and N_r^t includes the transbismuth r-process contributions. The Tl and Bi solar isotope abundances are from Ref. 1, the respective Hg and Pb abundances are determined via ^{198}Hg and ^{204}Pb, respectively, and the σN curve.

	$N_\odot$	N_s^1	N_r	
^{199}Hg	0.057±0.003	0.015 ±0.001	0.042±0.005	
^{200}Hg	0.079±0.005	0.050 ±0.006	0.028±0.009	
^{201}Hg	0.045±0.007	0.019 ±0.001	0.025±0.004	
^{202}Hg	0.101±0.009	0.077 ±0.006	0.024±0.015	
^{203}Tl	0.054±0.005	0.039 ±0.003	0.015±0.006	
^{204}Hg	0.024±0.002	0.003 ±0.0002[a]	0.021±0.002	
^{205}Tl	0.130±0.013	0.083 ±0.006	0.046±0.014	
	^{206}Pb	^{207}Pb	^{208}Pb	^{209}Bi
$N_\odot$	0.541±0.036	0.587 ±0.039	1.667±0.111	0.144 ±0.012
N_s^1	0.290±0.022	0.272 ±0.026	0.809±0.204	0.024 ±0.004
N_r	0.024±0.015	0.0068±0.0017[b]	0.024±0.015	0.0068±0.0017[b]
N_r^t	0.192±0.120	0.048 ±0.015[b]	0.144±0.090	0.081 ±0.026[b]
N_{rad}	0.04 ±0.02	0.223 ±0.054[b]	0.022±0.008	
N_s^2	0.02 ±0.13		0.69 ±0.25	
	0.033±0.017[b]	0.044 ±0.023[b]		0.039 ±0.023[b]

[a]Calculated assuming terrestrial half-life for ^{203}Hg.
[b]Calculated consistent with $N_s^2(^{208}\text{Pb})=(0.69\pm0.25)/10^6$ Si.

to 209. The radiogenic part from ^{238}U, ^{235}U, and ^{232}Th to ^{206,207,208}Pb can be calculated using one of the current r-process age determinations.[30–33]

It was Seeger *et al.*[21] who first showed that an exponential distribution of neutron exposures produces an adequate fit to the observed heavy s-process element abundances. These authors pointed out that the exponential distribution $\rho(\tau)\sim\exp(-\tau/\tau_0)$ of exposuress τ is a consequence of simple remixing models of the galaxy. The refined calculations[19,20,22–24] exhibited that a single value of the exposure parameter τ_0 cannot simultaneously produce the following:

the bulk s-process material between $A=100$ and 200;
the rapid increase of abundance towards iron as well as the pointed lead peak at $A=208$.[2,3]

While the iron slope requires a small exposure parameter τ_0, a strong value is needed for the lead peak compared to the τ_0 value of the bulk s-process material with mass numbers $100\leq A\leq 200$.

In the following we shall show that for the termination of s-process nucleosynthesis, a two-component fit is required with parameters τ_0 and τ_1 for the main and strong component, respectively.

With our measured capture cross sections and data from literature on ^{206,207,208}Pb, ^{209}Bi,[25–27] and especially on ^{204}Pb,[28] the size of the strong fluence component for ^{206,207,208}Pb and ^{209}Bi was calculated by subtracting from the solar abundances of these isotopes the main s process abundances and the various relevant r-process components.

The main s process through ^{206,207,208}Pb and ^{209}Bi and the α recycling via the Po isotopes have been calculated recently by Beer *et al.*[19] The s-process temperature kT and neutron density n_n were determined via selected branchings to be $kT=(18–28)$ keV and $n_n=(0.8–1.8)\times10^8$ cm^{-3}, respectively. This allows the calculation of the main s-process component of ^{206,207,208}Pb and ^{209}Bi and the solar lead abundance via the capture cross section of ^{204}Pb analogous to the mercury abundance determination with some confidence. From the good fit of s-only nuclei in the mass range $A=100–200$,[19] it is clear that the strong s-process component may contribute significantly only to isotopic abundances at ^{206,207,208}Pb and ^{209}Bi through sizable α recycling. Therefore, it is expected that ^{204}Pb is only little affected. The influence of the s-process branchings at ^{203}Hg and ^{204}Tl on ^{204}Pb is very small, as in both cases the beta decay rates are greatly increased due to nonunique first forbidden beta decay from excited states which is, in this mass region, as fast as an allowed transition. Because of the small capture cross section of ^{210}Po (Ref. 34) and the strong temperature sensitivity of the ^{210}Bi^m isomer,[3] practically no branching in the α recycling at the termination of the main s process occurs. In Table XII the various components of the studied isotopes are summarized. For lead a solar abundance of $(2.85\pm0.19)/10^6$ Si was obtained. This value is in agreement with the value of $3.15\pm0.25/10^6$ Si stated by Anders and Ebihara[1] from meteorites and the value $(2.3\pm0.5)/10^6$ Si determined from the spectrum of the sun.[35]

The subtraction of the main s process, the r process, and the radiogenic contributions from the solar abundances ^{206,207,208}Pb and ^{209}Bi are significant only for ^{208}Pb, as only in this case the strong s process is as dominant as the main s-process component. The radiogenic ^{208}Pb contribution from ^{232}Th is small because of the long half-life

of ^{232}Th, and the r process of ^{208}Pb [$(0.024\pm0.015)/10^6$ Si] estimated via N_r of ^{202,204}Hg [Fig. 9(b)] has to be multiplied only by six transbismuth progenitors. The various subtractions lead to a strong s-process abundance of $N_s^2(^{208}\text{Pb})=(0.69\pm0.25)/10^6$ Si. The corresponding calculations for ^{206}Pb yielded only an upper limit for the strong s-process component ($<0.15/10^6$ Si), and for the odd A isotopes ^{207}Pb and ^{209}Bi already the r-process contribution was difficult to estimate via ^{203,205}Tl [Fig. 9(b)]. For ^{207}Pb a dominant radiogenic contribution from ^{235}U is expected. A consistent description of the strong s process which reproduces ^{208}Pb offers the possibility to determine the radiogenic ^{207}Pb and use ^{235}U as a cosmic clock.

C. The strong s-process component and the ^{235}U cosmic clock

In order to investigate if the extra ^{208}Pb abundances [$(0.69\pm0.25)/10^6$ Si] can really be ascribed to a strong s-process exposure, we superimpose two exponential forms $\rho(\tau)$ according to the formalism given in Ref. 23:

$$\rho(\tau)=G_0\exp(-\tau/\tau_0)+G_1\exp(-\tau/\tau_1)\ , \tag{7}$$

with

$$G_{0,1}\tau_{0,1}=f_{0,1}N_\odot(56)\ .$$

The product $fN_\odot(56)$ stands for the number of seed nuclei, with $N_\odot(56)$ the solar abundance of ^{56}Fe and f the fraction of ^{56}Fe required as seed. The values $\tau_0=0.3$ mb^{-1}, $f_0=0.048\%$ represent the parameters of the σN curve which reproduces the bulk of heavy elements for $100\le A\le205$,[19] and τ_1,f_1 the parameters characterizing the strong exposure component. We have to attach as an additional condition to the strong fluence component the requirement that $\tau_1\gg\tau_0$ and $f_1\ll f_0$ which should ensure the production of ^{206,207,208}Pb and ^{209}Bi without appreciably affecting the σN curve at $A<206$.

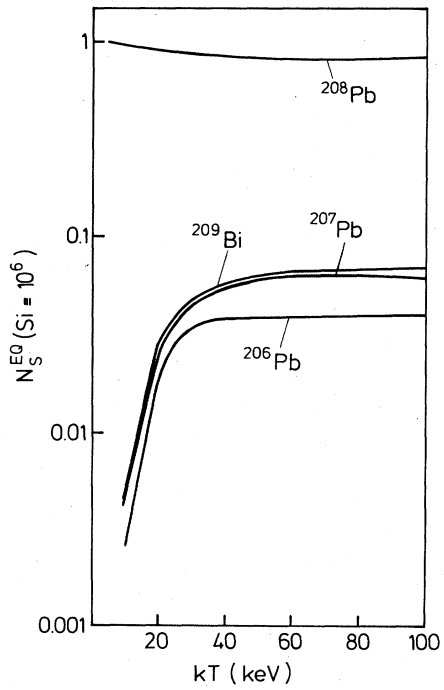

FIG. 8. The temperature dependence of the ^{206,207,208}Pb and ^{209}Bi abundances from the strong fluence component is illustrated for the equilibrium values.

In Fig. 7(b) it is demonstrated that this is the case. The iron seed $f_1N_\odot(^{56}\text{Fe})$ necessary to reproduce the ^{208}Pb abundance $N_s^2=(0.69\pm0.25)/10^6$ Si is plotted as a function of τ_1. On the right-hand ordinate the contribution of the strong s-process component to the main σN curve for $A<206$ is indicated. It is shown that the ^{208}Pb can be reproduced conveniently for $\tau>6$ mb^{-1} and $0.7\times10^{-6}<f_1<1.8\times10^{-6}$ only with an additional strong s-process contribution of $<2\%$ to the σN curve for $A<206$. In Fig. 7(a) the individual abundances of ^{206,207,208}Pb and ^{209}Bi as a function of τ_1 are shown. The nuclei ^{206,207}Pb are close to the equilibrium values for $\tau_1>6$ mb^{-1},[2] but this is different for ^{208}Pb and ^{209}Bi.

The calculations in Fig. 7 were performed for $kT=30$ keV. A variation of the temperature introduces an additional uncertainty. This is small for ^{208}Pb ($\pm5\%$) compared to the uncertainty in the experimental value of $N_s^2(^{208}\text{Pb})$ if we choose a reasonable temperature range of $kT=20$–60 keV (Fig. 8). For ^{206,207}Pb and ^{209}Bi the corresponding variation of the abundances is as large as the respective variation in the iron seed required to reproduce the ^{208}Pb abundance. Using our conditions for τ_1 and f_1, the strong s-process contributions for ^{206,207}Pb and ^{209}Bi are calculated. The values found are summarized in Table XII. Their uncertainties include both the uncertainty from $N_s^2(^{208}\text{Pb})$ and the uncertainty concerning the temperature of the strong component.

As ^{209}Bi has no radiogenic component, $N_\odot(^{209}\text{Bi})-N_s^1(^{209}\text{Bi})-N_s^2(^{209}\text{Bi})$ must be ascribed to the r process. This component of ^{209}Bi provides also a good approximation for the total r-process yield N_r^t of ^{207}Pb if it is properly weighted by the different numbers of transbismuth progenitors. As $N_r^t(^{207}\text{Pb})$ as well as $N_s^2(^{207}\text{Pb})$ are minor components of the solar ^{207}Pb abundance, the radiogenic ^{207}Pb is determined conveniently via

$$N_\odot(^{207}\text{Pb})-[N_s^1(^{207}\text{Pb})+N_s^2(^{207}\text{Pb})+N_r^t(^{207}\text{Pb})]$$

as $(0.223\pm0.054)/10^6$ Si.

Figure 9 shows a consistent analysis of lead and bismuth where the described procedure for the strong s-process component and the calculations of the main component from Ref. 19 have been applied.

With the ^{235}U abundance of $(0.005\,73\pm0.000\,48)/10^6$ (Ref. 1) and the ^{235}U decay rate λ, the r-process age can be calculated. Using Fowler's exponential model,

$$R=\frac{\lambda_r-\lambda}{\lambda_r}\frac{1-\exp(-\lambda_r\Delta)}{\exp(-\lambda\Delta)-\exp(-\lambda_r\Delta)}-1\ , \tag{8}$$

with $R=N_{\text{rad}}(^{207}\text{Pb})/N_\odot(^{235}\text{U})$ and where λ_r is the supernova rate with $\lambda_r\Delta=1/0.43$, the r-process age T was found to be $T=4.6$ Gyr $+\Delta=17.2\pm2.6$ Gyr. Δ is the time duration of the r process.

This value is in excellent agreement with the r-process age reported by Thielemann[30,36] ($T=17.6\pm4.0$ Gyr). Other earlier r-process age determinations[31–33] are some-

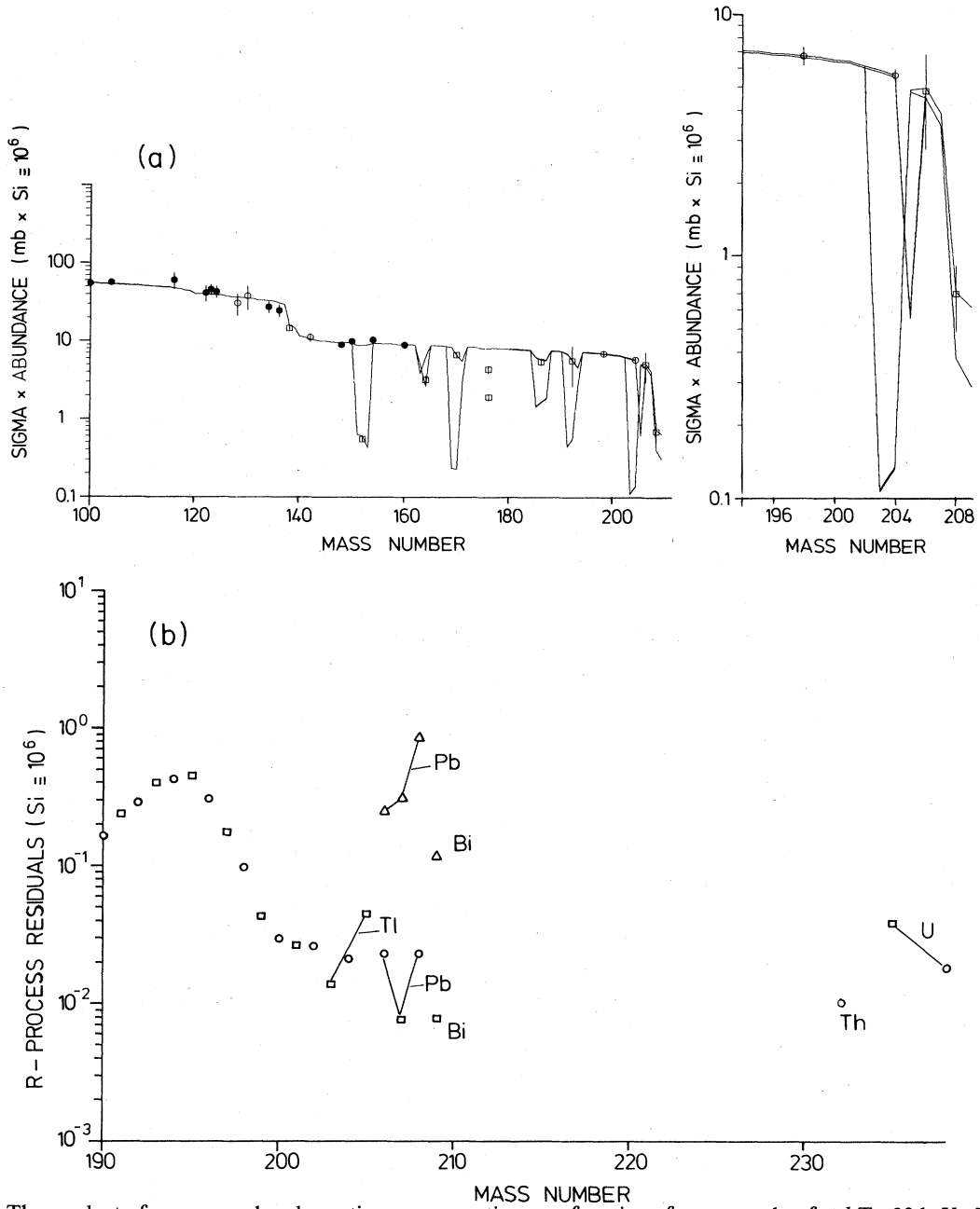

FIG. 9. (a) The product of s-process abundance times cross section as a function of mass number for $kT=23$ keV. The solid line is the result of the s-process calculation. The influence of the strong component is negligible, except above $A=206$. This is better visible on an extended scale (insert). The lower curve in the insert is the main component only, the upper curve the sum of main plus strong component. The symbols correspond to empirical values for s-only isotopes or to s-process-dominated isotopes near magic neutron shells. Significant branchings were identified due to the low empirical σN values ^{152}Gd, ^{164}Er ^{170}Yb, ^{186}Os, and ^{192}Pt. The ^{198}Hg and ^{204}Pb are normalized to the σN curve. The branchings at ^{203}Hg, ^{204}Tl, and ^{205}Pb are treated using neutron density and temperature from the other branchings. The half-life of ^{203}Hg is assumed to be terrestrial. (b) r-process abundances are derived by subtracting the s-process components from the solar abundances. Note that Pb, Bi, U, and Th have been corrected for short-lived progenitors and the radioactive U and Th decay since r-process formation. The decomposition is consistent with the expected flat r-process abundance distribution for isotopes $202 \leq A \leq 238$. The abundances of ^{206,207,208}Pb and ^{209}Bi with the main s-process component subtracted are shown too (open triangles).

what lower but still compatible within the quoted uncertainties. These older values have been, however, questioned in the light of new evidence.[30,37,38]

As the half-life of ^{235}U is short compared to Δ, the ^{235}U clock is sensitive to the time history of the r-process production function. Therefore, if we adopt $\Delta=13\pm4$ Gyr from Thielemann,[30] we can estimate $\lambda_r\Delta$ as $1.197 \leq \lambda_r\Delta \leq 3.520$. This means that within the framework of

the exponential model, the production rate of r-process nuclei at the time of solar system formation was only $(10.5^{+19.7}_{-7.5})\%$ of the initial rate.

VI. CONCLUSIONS

We have measured and analyzed the neutron capture cross sections of the stable mercury isotopes. Average resonance parameters were determined and Maxwellian averaged capture cross sections calculated. The capture cross section of ^{198}Hg yielded, in conjunction with an analysis of the main s-process nucleosynthesis, the solar mercury abundance, and the capture cross sections of ^{199,200,201,202,204}Hg allowed the decomposition of their isotope abundances into the s- and r-process components.

The r-process distribution curve from $A=199$ to 204 lead us to an estimate of the r-process components of ^{206,208}Pb. In this way an important prerequisite for a consistent analysis of the termination of the s process was obtained. A further step formed the determination of the lead abundance similar to the procedure used for mercury. Within the quoted uncertainties the value obtained was in agreement with the Pb solar abundance from meteorite analysis[1] and the spectrum of the sun.[35] The decomposition of ^{208}Pb according to the different processes of nucleosynthesis showed that a sizable abundance contribution is *not* accounted for either by the main s process or the r process or the radiogenic ^{232}Th contribution. However, the adoption of an extra s-process component, a strong fluence component, can explain consistently this additional ^{208}Pb abundance. The s process from this strong fluence exposure is near its equilibrium value for ^{206,207}Pb.

The reproduction of ^{208}Pb yielded constraints for the necessary iron seed and the average time integrated neutron flux τ_1 of this component. A fraction f_1 of solar ^{56}Fe between $(0.7-1.8)\times10^{-6}$ and $\tau_1>6$ mb^{-1} are required. These values were sufficiently accurate to consistently decompose ^{209}Bi and ^{206}Pb and to determine the radiogenic ^{207}Pb abundance for an investigation of the ^{235}U cosmic clock. The calculated r-process age is in excellent agreement with the result reported by Thielemann.[30] This agreement is remarkable, as our approach to determine the original ^{235}U abundance is quite different from the analysis of Thielemann *et al.*[29] In Ref. 29 an r-process calculation is performed, whereas in this work the radiogenic ^{207}Pb is determined similar to a suggestion of Clayton.[39] It should also be noted that Thielemann's[30] r-process age is mainly based on the two long-lived radionuclides ^{238}U and ^{232}Th, contrary to the present study performed on ^{235}U.

ACKNOWLEDGMENTS

We would like to thank E. Anders for his information concerning the solar abundances of lead and bismuth. The assistance of B. J. Allen and the ORELA operation staff in data taking is gratefully acknowledged. One of us (H.B.) is grateful to the U. S. Department of Energy for funding a story at ORNL to carry out this work.

[1] E. Anders and M. Ebihara, Geochim. Cosmochim. Acta **46**, 2363 (1982).
[2] D. D. Clayton and M. E. Rassbach, Astrophys. J. **148**, 69 (1967).
[3] R. A. Ward and D. D. Clayton (unpublished).
[4] R. L. Macklin, Nucl. Instrum. Methods **91**, 79 (1971).
[5] R. L. Macklin and J. H. Gibbons, Phys. Rev. **159**, 1007 (1967).
[6] J. B. Czirr, Nucl. Instrum. Methods **72**, 23 (1969).
[7] R. L. Macklin and B. J. Allen, Nucl. Instrum. Methods **91**, 565 (1971).
[8] R. L. Macklin, J. Halperin, and R. R. Winters, Nucl. Instrum. Methods **164**, 213 (1979).
[9] R. L. Macklin and R. R. Winters (unpublished).
[10] R. L. Macklin, Nucl. Instrum. Methods **26**, 213 (1964).
[11] R. L. Macklin, Nucl. Instrum. Methods **59**, 12 (1976).
[12] F. H. Fröhner (unpublished).
[13] R. L. Macklin, Nucl. Sci. Eng. **86**, 362 (1984).
[14] R. L. Macklin and J. H. Gibbons, Rev. Mod. Phys. **37**, 166 (1965).
[15] J. E. Ross and L. H. Aller, Science **191**, 1223 (1976).
[16] A. G. W. Cameron, in Essays in Nuclear Astrophysics, edited by C. A. Barnes, D. D. Clayton, and D. N. Schramm (Cambridge University Press, Cambridge, 1983), p. 23.
[17] H. Palme, H. Suess, and H. D. Zeh, in *Astronomy and Astrophysics,* Vol. 2, edited by K. Schaifers and H. H. Voigt, Landolt-Börnstein (Springer, Berlin, 1981), p. 257.
[18] G. Walter and H. Beer, Astron. Astrophys. **123**, 279 (1983).
[19] H. Beer, G. Walter, R. L. Macklin, and P. J. Patchett, Phys. Rev. C **30**, 464 (1984).
[20] F. Käppeler, H. Beer, K. Wisshak, D. D. Clayton, R. L. Macklin, and R. A. Ward, Astrophys. J. **257**, 821 (1982).
[21] P. A. Seeger, W. A. Fowler, and D. D. Clayton, Astrophys J. Suppl. Ser. **11**, 121 (1965).
[22] R. K. Ulrich, in *Explosive Nucleosynthesis,* edited by D. N. Schramm and W. D. Arnett (University of Texas Press, Austin, 1973), p. 139.
[23] R. A. Ward, M. J. Newman, and D. D. Clayton, Astrophys. J. Suppl. Ser. **31**, 33 (1976).
[24] R. A. Ward and M. J. Newman, Astrophys. J. **219**, 195 (1978).
[25] B. J. Allen, R. L. Macklin, R. R. Winters, and C. Y. Fu, Phys. Rev. C **8**, 1504 (1973).
[26] R. L. Macklin, J. Halperin, and R. R. Winters, Astrophys. J. **217**, 222 (1977).
[27] R. L. Macklin and J. Halperin, Phys. Rev. C **14**, 1389 (1976).
[28] D. J. Horen, R. L. Macklin, J. A. Harvey, and N. W. Hill, Phys. Rev. C **29**, 2126 (1984).
[29] F.-K. Thielemann, J. Metzinger, and H. V. Klapdor, Z. Phys. A **309**, 301 (1983).
[30] F.-K. Thielemann, in Proceedings of the 2nd Workshop On Nuclear Astrophysics, Ringberg Castle, 1983, Report MPA 90, 1983.
[31] S. E. Woosley and W. A. Fowler, Astrophys. J. **233**, 411 (1979).
[32] J. C. Browne and B. L. Berman, Phys. Rev. C **23**, 1434 (1981).
[33] R. R. Winters and R. L. Macklin, Phys. Rev. C **25**, 208 (1982).
[34] M. J. Harris, Astrophys. Space Sci. **77**, 357 (1981).
[35] O. Hauge and H. Sorli, Sol. Phys. **30**, 301 (1973).

[36]W. A. Fowler, Rev. Mod. Phys. **56**, 149 (1984).
[37]K. Yokoi, K. Takahashi, and M. Arnould, Astron. Astrophys. **117**, 65 (1983).
[38]M. Arnould, K. Takahashi, and K. Yokoi, Astron. Astrophys. **137**, 51 (1984).
[39]D. D. Clayton, Astrophys. J. **139**, 637 (1964).